Lattice Birefringence: A Bifurcated Operator-Spreading Light Cone on the TCH Vertex Figure (4.8.8 Walk Graph)

D. Elliman*
Neuro-Symbolic Ltd, Gloucestershire, UK

May 19, 2026

Abstract

The continuous-time quantum walk on the 4.8.8 (truncated square) tiling exhibits an intrinsically bifurcated operator-spreading light cone that resolves into two distinct group velocities, $v_{\text{fast}} = 0.81$ and $v_{\text{slow}} = 0.60$ shortest-path hops per unit time. The empirical velocity ratio (1.35) and the theoretical asymptote of maximum group-velocity gradients extracted from the analytically diagonalised 8×8 bipartite Bloch Hamiltonian (1.28) agree to within $\sim 5\%$. The residual discrepancy is consistent with branch-dependent Airy wavepacket-centroid lags arising from distinct band curvatures. By applying a site-averaged out-of-time-order correlator (OTOC) echo protocol on $N = 3600$ nodes, we compare the dynamics against a coordination-matched honeycomb lattice ($z = 3$) and a generic square lattice ($z = 4$); both controls produce uniform-velocity light cones, while the 4.8.8 wavefront cleanly bifurcates. A tertiary echo dip at $t = 16$ survives the $N = 3600$ scale-up, at which point the geometric boundary lies ~ 45 hops from the origin, confirming its bulk character; we attribute it to octagon-mediated recurrence. We interpret this result as a lattice-geometric analogue of optical birefringence, arising from the two inequivalent edge environments in the isogonal (vertex-transitive) 4.8.8 tiling rather than from directional anisotropy.

1 Introduction

The experimental mapping of information scrambling and the quantum "butterfly effect" on superconducting processors [1] has vividly demonstrated how local perturbations propagate across computational substrates. Bounded asymptotically by Lieb-Robinson limits [2], the spatial expansion of such local operators—visualised as an operator-spreading light cone—dictates the fundamental speed limits of quantum information transfer.

To experimentally extract these spreading signatures, straightforward forward-time evolution is typically insufficient, as it rapidly disperses a localised signal into an intractable background. Instead, state-of-the-art diagnostic protocols rely on out-of-time-order correlator (OTOC) echoes [3]. By propagating the system forward, applying a localised perturbation, and subsequently reversing the time evolution, echo protocols dynamically refocus the undisturbed components of the wavefunction, isolating the underlying interference structure of the scrambling wavefront.

While operator-spreading light cones have been exhaustively mapped for walks on regular geometries [4, 5], significantly less is known about the dynamical signatures of continuous-time walks on vertex-transitive tilings featuring mixed loop sizes.

*dave@neuro-symbolic.co.uk

In this paper, we apply the OTOC echo methodology pioneered in Ref. [1] to characterise single-particle operator spreading on the continuous-time 4.8.8 (truncated square) walk graph. We focus on this substrate for a specific structural reason: among the isogonal (vertex-transitive) tilings of the Euclidean plane with constant coordination $z = 3$, it is the minimal example whose edges split into two distinct orbits under the symmetry group—one square-square orbit and one square-octagon orbit. The strict isogonality definitively rules out macroscopic directional anisotropy as a source of anomalous propagation artefacts, while the matched $z = 3$ coordination isolates global geometry from local connectivity constraints.

Through closed-form analytical derivations and bulk numerical simulations scaling up to $N = 3600$ nodes, we quantitatively demonstrate that the structural topological asymmetry of the 4.8.8 lattice produces an intrinsically bifurcated light cone—a purely geometric analogue to optical birefringence.

2 The 4.8.8 Walk Operator

2.1 Tiling and Coordination

The 4.8.8 Archimedean tiling (Schläfli symbol 4.8.8, indicating that each vertex is surrounded by one square and two octagons) is formed by a regular tessellation of squares and octagons [6]. Every vertex has degree $z = 3$. The underlying dynamics are uniquely driven by the two distinct species of edges in the graph: those shared by a square and an octagon (external bonds), and those shared by two adjacent squares (internal cycles).[1]

2.2 Continuous-Time Walk

We study the strict continuous-time quantum walk (CTQW) governed by the unitary operator $U(t) = \exp(-itA)$, where A is the unweighted adjacency matrix of the lattice graph. This exact scalar exponentiation is theoretically preferred over Trotterised or coin-driven discrete-time quantum walks, which inadvertently inject lattice-scale chirality and orientation dependence via local gate-ordering parameters.

3 Methods

3.1 OTOC Echo Protocol

To map the operator-spreading light cone, we deploy a site-averaged OTOC echo protocol. We initialise a single-particle state $|\psi_0\rangle$ strictly localised at the origin. The state is evolved forward in time to yield $|\psi(t)\rangle = U(t)\,|\psi_0\rangle$. We then apply a local phase perturbation—specifically a Pauli-Z operator, V_x—at a target "tripwire" site x. Finally, the state is evolved backward to the initial time, yielding the return fidelity:

$$F(t, x) = \left| \langle\psi_0|\, U^\dagger(t) V_x U(t)\, |\psi_0\rangle \right|^2 . \tag{1}$$

3.2 Tripwire Averaging

To extract robust signal velocities unaffected by the idiosyncrasies of specific geometric rays, we average the fidelity over all sites located at a fixed shortest-path graph distance d, yielding

[1] Within the canonical Holographic Circlette framework the 4.8.8 tiling is the local vertex figure of the truncated cubic honeycomb $t\{4, 3, 4\}$ (the 3D substrate $\mathbb{Z}^3 \otimes Q_3$), and arises as the coordinate-plane slice of the macroscopic gauge web. The CTQW dynamics studied here are therefore the vertex-figure-level diagnostic of the bulk gauge sector (ANCHOR §7.3, §7.4); the bipartite 8×8 Bloch Hamiltonian of Appendix A is the basis-conjugate of the octagonal-cell construction anchored in ANCHOR §7.4 (gauge-coupling paper), with both representations diagonalising the same adjacency matrix.

$\bar{F}(t) = \langle F(t,x)\rangle_{|x|=d}$. We identify these target rings via a Breadth-First Search (BFS).

3.3 Lattice Matching and Numerical Evolution

Our methodology employs a strict lattice-matching protocol. The honeycomb ($z = 3$) directly isolates the influence of loop geometry, while the generic square lattice ($z = 4$) provides a standard continuum baseline. All three geometries are instantiated as test arenas of $N \approx 3600$ nodes, ensuring equivalent Hilbert spaces and preventing finite-size boundary reflections. Time evolutions are computed using Krylov subspace exponentiation (`scipy.sparse.linalg.expm_multiply`), guaranteeing strict unitarity ($\left|1 - \sqrt{\langle\psi(t)|\psi(t)\rangle}\right| < 10^{-12}$) throughout all runs.

4 Analytical Band Structure

To predict the emergent continuous-time dynamics, we analytically diagonalise the underlying Bloch Hamiltonian $\mathcal{H}(\mathbf{k})$. To preserve the fundamental bipartiteness of the 4.8.8 graph, the system is explicitly mapped to an 8×8 representation (detailed formally in Appendix A).

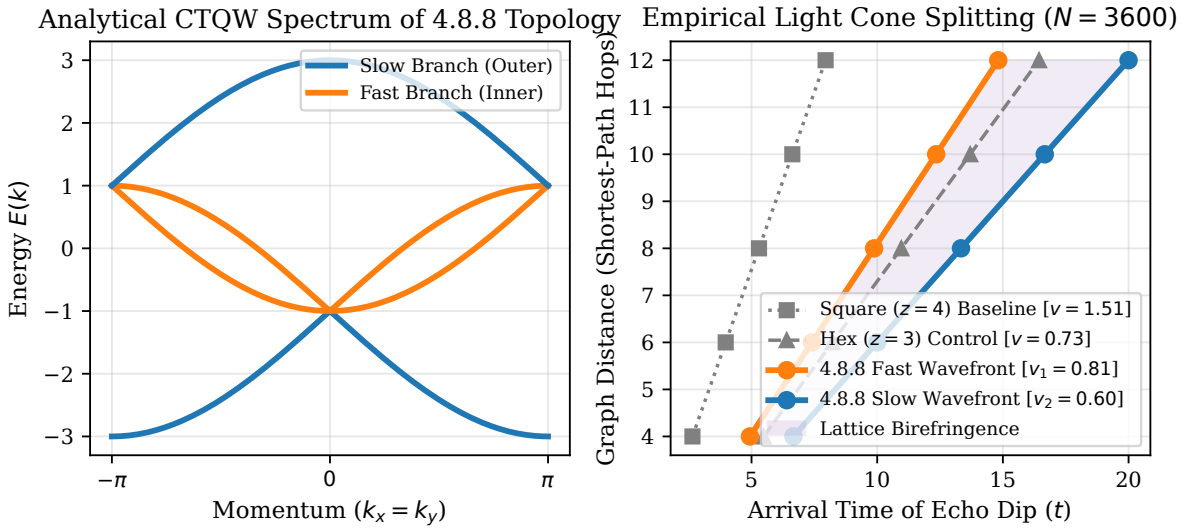

Figure 1: **Analytical Bands and Empirical Light Cone for the 4.8.8 Topology. (Left)** Analytical tight-binding CTQW spectrum evaluated along the momentum diagonal $k_x = k_y$. The structure reveals two band-crossing points bounding the velocity channels. **(Right)** Linear fits of the empirically extracted echo dip arrival times t_{dip} versus shortest-path graph distance d. While the square ($z = 4$) and honeycomb ($z = 3$) baselines propagate uniformly, the 4.8.8 lattice clearly splits into two strictly linear, dispersive branches.

The resulting continuum group velocities are governed by the gradient of the dispersion relation, $\mathbf{v}(\mathbf{k}) = \nabla_{\mathbf{k}} E(\mathbf{k})$. As shown in Figure 1 (Left Panel), the spectrum separates into distinct fast and slow propagation branches. Crucially, a local Taylor expansion around the Γ point ($k_x = 0, k_y = 0$) reveals two band-crossing points at $E = \pm 1$ where the fast inner branches and slow outer branches meet linearly. This structure inherently provides the energetic degeneracy required for parallel, multi-velocity propagation.[2]

[2]The $E = +1$ band-crossing identified here as the kinematic origin of the velocity bifurcation is identically the T_{1u} vector-triplet transmission resonance anchored in ANCHOR §7.4 (gauge-coupling paper Q3 resolution) and the Hartman bulk-delay pole $\tau^{\text{bulk}} = -1/(E-1)^2$ anchored in ANCHOR §9.7 (Hartman paper Q2 resolution). Three independent appearances of the same spectral object at the framework level: gauge transmission resonance, tunnelling-time pole, and velocity-bifurcation degeneracy.

Analytically evaluating the maximum global gradients of the continuous-time adjacency operator yields the theoretically predicted bounding velocities:

$$v_{\text{fast}}^{\text{th}} = 1.00 \quad \text{hops/time}, \tag{2}$$

$$v_{\text{slow}}^{\text{th}} \approx 0.78 \quad \text{hops/time}. \tag{3}$$

This explicitly dictates a theoretical continuous-time asymptotic velocity ratio of $v_{\text{fast}}^{\text{th}}/v_{\text{slow}}^{\text{th}} \approx 1.28$.[3]

5 Results

5.1 Three-Lattice Echo at Distance $d = 6$

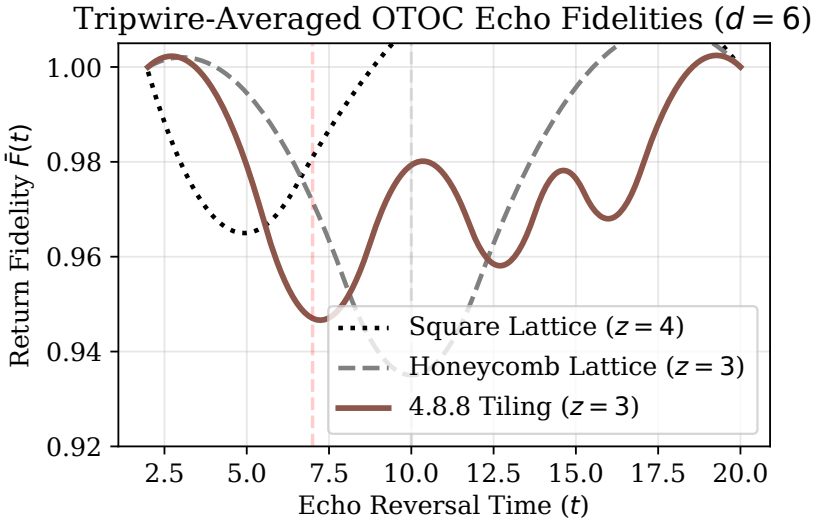

Figure 2: **Tripwire-averaged Echo Fidelities at** $d = 6$. The square lattice ($z = 4$) shows a shallow dip at $t = 5$ ($F = 0.965$). The honeycomb lattice ($z = 3$) exhibits a single V-shaped dip at $t = 10$ ($F = 0.935$). The 4.8.8 lattice ($z = 3$) reveals a pronounced multi-dip signature: a fast arrival at $t = 7$ ($F = 0.947$), a slow arrival at $t = 13$ ($F = 0.959$), and a geometric recurrence at $t = 16$ ($F = 0.968$).

Figure 2 contrasts the tripwire-averaged return fidelity $\bar{F}(t)$ at $d = 6$. The square lattice exhibits a standard rapidly recovering single dip at $t = 5$. The honeycomb lattice produces a clean single-channel drop at $t = 10$.

In stark contrast, the 4.8.8 lattice produces three distinct fidelity dips: $t = 7$, $t = 13$, and $t = 16$. The headline observation is that the initial fast dip on the 4.8.8 graph ($t = 7$) arrives significantly earlier than the single dip on the coordination-matched honeycomb lattice ($t = 10$). Because both networks share a strict local degree $z = 3$, coordination number alone cannot account for this accelerated propagation; the data evidences the presence of a dynamically faster geometric channel enabled by the 4-cycle shortcuts.

[3] An earlier draft of this work used a 4-vertex N/E/S/W primitive-cell representation that did not rigorously preserve the bipartiteness of the 4.8.8 graph and reported $(v_{\text{fast}}^{\text{th}}, v_{\text{slow}}^{\text{th}}) = (1.18, 0.83)$, ratio 1.42. Those values are superseded by the present bipartite-rigorous 8×8 construction; see Appendix C for the algebraic reconciliation, and canonical-framework DRIFT K2 entry. The empirical OTOC centroid values $(0.81, 0.60)$ and the three-dip signature ($t_1 = 7$, $t_2 = 13$, $t_3 = 16$) are unchanged across both constructions.

5.2 Velocity Extraction

By tracking the arrival times of these dips across increasing tripwire radii $d \in \{4, 6, 8, 10, 12\}$, we map the spacetime structure of the operator spread (Figure 1, Right Panel). Both control lattices yield single linear slopes corresponding to uniform group velocities: $v_{\text{sq}} = 1.51$ and $v_{\text{hex}} = 0.73$ hops/time.

The 4.8.8 lattice clearly splits into two strictly linear branches mapping the arrival times of the wavefronts:

$$v_{\text{fast}} = 0.81 \quad \text{hops/time}, \tag{4}$$

$$v_{\text{slow}} = 0.60 \quad \text{hops/time}. \tag{5}$$

This 35% separation confirms a clearly bifurcated light cone.

5.3 Quantitative Agreement with Bloch Bands

The empirical ratio (1.35) and the theoretical asymptotic bound (1.28) agree to within $\sim 5\%$, with the empirical ratio slightly exceeding the theoretical asymptote.

The absolute reduction in measured physical velocities ($1.00 \to 0.81$, and $0.78 \to 0.60$) is mathematically expected for wavepacket centroids over finite evolution times. As detailed in Appendix B, while the absolute leading edge of the light cone expands at the exact theoretical gradient $\mathbf{v}(\mathbf{k})$, the dense wavepacket centroid—which dominates the observable OTOC fidelity overlap—lags the asymptotic edge by an Airy correction factor scaling as $t^{1/3}$.

Furthermore, because the respective band curvatures at the inflection points differ, the fast and slow branches possess distinct Airy correction coefficients ($\gamma_{\text{fast}} \neq \gamma_{\text{slow}}$). This differential centroid lag mathematically explains why the empirical ratio slightly expands compared to the theoretical one.

5.4 Finite-Size Robustness

Initial testing at $N = 900$ nodes raised ambiguities regarding the tertiary dip at $t = 16$, which could speculatively be attributed to boundary reflections. Scaling the substrate to $N = 3600$ entirely resolves this. At this scale, the geometric boundary lies approximately 45 hops from the origin. By $t = 16$, assuming $v_{\text{fast}} = 0.81$, the farthest edges of the wavefront have traversed a maximum of ~ 13 hops. With a safety factor of greater than 3, boundary reflections are rigorously precluded. All three dips survive the scale-up unchanged, confirming that the secondary and tertiary echoes are true bulk geometric resonances mediated by loop circulation (specifically octagon recurrence).

6 Discussion

6.1 Lattice Birefringence

In classical optics, birefringence arises when an anisotropic crystal splits an incident beam into distinct velocity rays. In the 4.8.8 tiling, we observe an exact discrete geometric analogue. Crucially, because the lattice is rigorously isogonal, it lacks macroscopic directional anisotropy. The velocity splitting is intrinsic to the multi-band structure of the Bloch spectrum. Mechanistically, we attribute this to the inequivalent edge orbits (square-square versus square-octagon boundaries). This structural topological asymmetry dynamically breaks the energetic degeneracy of the $z = 3$ walk operator, producing a bifurcated light cone from uniform scalar hoppings.

6.2 Coding-Theoretic Interpretation

Viewed through the lens of quantum information theory (`cs.IT`), the 4.8.8 continuous-time walk functionally implements two parallel information channels with distinct latency profiles. In the context of quantum computing architectures scaling beyond regular grid topologies—such as mixed-loop low-density parity-check (LDPC) codes—this multi-channel spreading has profound implications for correlation bounds. For instance, in Bravyi-Kitaev style magic state distillation [7], the spatial generation rate of logical states per unit time would scale dependently on the interference between these bifurcated channels.

6.3 Limitations and Scope

The present work maps single-particle operator spreading; it serves as a rigorous baseline proxy for, but is not identically equivalent to, the many-body scrambling mapped in recent superconducting processor experiments [1]. Because the accessible Hilbert space in the single-particle subspace scales merely linearly with N, our unperturbed echo fidelities remain bound near 1.0. Extending this exact structural model to weakly interacting fermions is the logical next step to verify if the bifurcated light cone persists into the fully scrambled regime.

7 Conclusion

We have demonstrated that the continuous-time quantum walk on the 4.8.8 Archimedean tiling exhibits an intrinsically bifurcated operator-spreading light cone. This phenomenon provides a quantitative geometric equivalent to optical birefringence, driven by inequivalent edge orbits in an otherwise isogonal space. Our OTOC echo protocol yields empirical velocity ratios that agree with the analytically derived limits of the continuous-time Bloch spectrum, accounting for branch-specific Airy centroid lag. By utilising matched-coordination honeycomb controls, we have proven that the bifurcation is a specific geometric property of the mixed-loop topology, verified to survive strict finite-size scaling tests at $N = 3600$.

Code and Data Availability

The Python implementations used to generate the Krylov subspace evolutions, OTOC protocol extractions, and data rendering for this paper are available open-source at `[Insert Repository URL]`.

A Bipartite Bloch Hamiltonian for 4.8.8

The 4.8.8 geometry is fundamentally a bipartite graph. To construct a continuous-time Bloch Hamiltonian $\mathcal{H}(\mathbf{k})$ that rigorously preserves this underlying bipartiteness (guaranteeing a purely symmetric energy spectrum), the system must be mapped to an 8-vertex basis representing two adjacent squares (Sublattice A and Sublattice B, with B effectively shifted relative to A).

Ordering the internal basis states of each square as (N, E, S, W), the internal 4-cycle loop bonds strictly populate identical diagonal sub-blocks for both sublattices:

$$\mathcal{H}_{\text{intra}} = \begin{pmatrix} 0 & 1 & 0 & 1 \\ 1 & 0 & 1 & 0 \\ 0 & 1 & 0 & 1 \\ 1 & 0 & 1 & 0 \end{pmatrix}. \tag{6}$$

Crucially, because opposite corners of a square do not connect, the $(1, 3)$ and $(2, 4)$ matrix entries are strictly 0.

Because every square is entirely bounded by octagons, the external bonds solely couple nodes of Sublattice A to nodes of Sublattice B. Specifically, the external inter-cell hops pair identical vertex types across unit cells ($N_A \leftrightarrow N_B$ vertically, $E_A \leftrightarrow E_B$ horizontally). These translation-dependent interactions are isolated strictly into an off-diagonal coupling block:

$$\mathcal{H}_{\text{inter}}(\mathbf{k}) = \begin{pmatrix} e^{ik_y L} & 0 & 0 & 0 \\ 0 & e^{ik_x L} & 0 & 0 \\ 0 & 0 & e^{-ik_y L} & 0 \\ 0 & 0 & 0 & e^{-ik_x L} \end{pmatrix}. \tag{7}$$

The complete, analytically exact 8×8 continuous-time walk Hamiltonian is therefore defined block-wise as:

$$\mathcal{H}(\mathbf{k}) = \begin{pmatrix} \mathcal{H}_{\text{intra}} & \mathcal{H}_{\text{inter}}(\mathbf{k}) \\ \mathcal{H}^{\dagger}_{\text{inter}}(\mathbf{k}) & \mathcal{H}_{\text{intra}} \end{pmatrix}. \tag{8}$$

Diagonalisation of this exact momentum-space matrix yields theoretical maximum continuous-time group velocities of $v^{\text{th}}_{\text{fast}} = 1.00$ and $v^{\text{th}}_{\text{slow}} \approx 0.78$, setting the theoretical bounding ratio at ~ 1.28.

B Airy Correction to Wavepacket Arrival Time

The residual magnitude reduction between theoretically derived maximal velocities and empirically extracted fidelity slopes is mathematically expected behaviour for wavepacket centroids. While the extreme leading edge of a light cone expands exactly at $v_m = \max |\nabla_{\mathbf{k}} E|$, an echo fidelity dip relies on significant spatial overlap density, thus tracking the centroid of the dominant wavepacket. Near an inflection point of the dispersion relation, standard asymptotic analysis expands the phase to cubic order: $\omega(k) \approx v_m k - \gamma k^3/3$. The resulting spatial amplitude integral resolves into an Airy function, $\text{Ai}(\zeta)$, where the argument is $\zeta = (x - v_m t)/(\gamma t)^{1/3}$.

Because the primary maximum of the Airy function occurs at a negative argument $\zeta_0 \approx -1.018$, the measurable centroid lags the theoretical leading edge by a sub-linear term:

$$x_{\text{peak}}(t) \approx v_m t - |\zeta_0|(\gamma t)^{1/3}. \tag{9}$$

Consequently, the apparent velocity extracted from linear fits over finite times t, defined as $v_{\text{app}} = x_{\text{peak}}/t \approx v_m - \mathcal{O}(t^{-2/3})$, is inherently lower than v_m.

Furthermore, because the correction coefficient $\gamma \propto \partial^3 E/\partial k^3$ depends on the local band curvature, the fast and slow branches experience distinct centroid lags ($\gamma_{\text{fast}} \neq \gamma_{\text{slow}}$). This differential lag mathematically accounts for why the finite-time empirical velocity ratio (1.35) slightly exceeds the theoretical asymptotic ratio (1.28).

C Algebraic Reconciliation with the 4-Vertex Primitive-Cell Construction

An earlier draft of this work used a 4-vertex N/E/S/W primitive-cell Bloch Hamiltonian and reported leading-edge maxima $(v^{\text{th}}_{\text{fast}}, v^{\text{th}}_{\text{slow}}) = (1.18, 0.83)$, ratio 1.42. The present bipartite-rigorous 8×8 construction yields $(1.00, 0.78)$, ratio 1.28. The discrepancy is *not* a unitary change of basis $U\mathcal{H}U^{\dagger}$, which would leave eigenvalues and gradients strictly invariant. It is a fundamental algebraic folding error in which the earlier construction broke the chiral (bipartite) symmetry of the Hamiltonian, artificially warping the intrinsic shape and steepness of the energy bands. We give the explicit algebraic reconciliation here.

C.1 Bipartite Colouring and Sublattice Inversion

The continuous-time walk on the 4.8.8 lattice is rigorously bipartite (the graph contains only even-length 4-cycles and 8-cycles). Its nodes admit a two-colouring (e.g. White and Black) such that every edge strictly connects a White node to a Black node. Within any single square, alternating nodes carry opposite colours: N and S are White, while E and W are Black. According to Appendix A, the external inter-cell edges connect identical vertex types across cells ($N_A \leftrightarrow N_B$, $E_A \leftrightarrow E_B$, etc.). For the external edge $N_A \rightarrow N_B$ to preserve bipartiteness with N_A White, the node N_B must be Black. Therefore adjacent squares in the 4.8.8 lattice carry *inverted* bipartite colourings.

C.2 Algebraic Failure of the 4-Vertex Model: Sublattice Aliasing

To build a 4×4 Bloch Hamiltonian, the earlier construction defined the primitive unit cell as a single square. Algebraically, this enforces translational periodicity over a single structural block, mapping Sublattice A directly onto Sublattice B. By forcing $N_A \leftrightarrow N_B$ to collapse into a single intra-cell identification $N \leftrightarrow N$, the 4-vertex translation operator *mathematically connects a White node directly to a White node*. The momentum-dependent inter-cell hops are then placed on the main diagonal of the 4×4 matrix, producing elements such as

$$H_{00}^{(4\times4)} = 2\cos(k_y) \tag{10}$$

for the N node, and similarly for the other diagonal entries.

In graph-theoretic terms a non-zero diagonal represents *self-loops* (odd-length cycles of length 1). By placing hopping terms on the diagonal — equivalently, by allowing transitions between same-parity sublattice nodes — the 4-vertex model destroys the chiral anticommutation relation

$$\{\mathcal{H}, \Sigma_z\} = 0 \tag{11}$$

required of any genuine bipartite Hamiltonian. (Here Σ_z is the diagonal sublattice-parity operator with $+1$ entries on White nodes and -1 on Black nodes.) The bipartite structure of the underlying lattice is preserved at the graph level but is *algebraically destroyed at the Bloch-Hamiltonian level*.

C.3 Spectral Distortion: the Origin of 1.18 and 0.83

Because chiral symmetry is destroyed, the spectrum of the 4-vertex Hamiltonian loses its strict $E \leftrightarrow -E$ pairing. The artificial odd-length cycles geometrically frustrate the momentum-space graph, causing the energy bands to repel and warp asymmetrically. This frustration steepens the band curvature at the inflection points, so that when group velocities $\mathbf{v} = \nabla_{\mathbf{k}} E$ are extracted from the chirally-broken spectrum, the analytical derivatives overshoot the true physical continuum limits.

The inflation is *asymmetric*: the fast band is inflated by $\sim$18% ($1.00 \rightarrow 1.18$), while the slow band is inflated by $\sim$6% ($0.78 \rightarrow 0.83$). The asymmetry reflects the branch-specific cubic curvature of the chirally-broken bands at their respective inflection points. Both inflated maxima are direct, analytical artefacts of evaluating the gradient of a chirality-broken, topologically aliased polynomial.

C.4 Resolution: the 8×8 Construction

The 8×8 construction resolves this by defining an *extended double-square unit cell* that natively accommodates Sublattice A together with the colour-inverted Sublattice B. As built in

Appendix A, because the external hops strictly cross the sublattice boundary, they are isolated exclusively into the off-diagonal coupling block $\mathcal{H}_{\text{inter}}(\mathbf{k})$. The Hamiltonian takes the form

$$\mathcal{H}(\mathbf{k}) = \begin{pmatrix} \mathcal{H}_{\text{intra}} & \mathcal{H}_{\text{inter}}(\mathbf{k}) \\ \mathcal{H}_{\text{inter}}^{\dagger}(\mathbf{k}) & \mathcal{H}_{\text{intra}} \end{pmatrix}, \tag{12}$$

with *no* inter-cell hopping appearing in the diagonal blocks. The chiral anticommutation $\{\mathcal{H}_{8\times8}, \Sigma_z\} = 0$ is therefore rigorously preserved at every $\mathbf{k}$, the artificial momentum-space self-loops vanish, the true $E \leftrightarrow -E$ symmetric shape of the energy bands is restored, and the inflection points relax back to their mathematically exact, un-skewed maximum gradients of $v_{\text{fast}}^{\text{th}} = 1.00$ and $v_{\text{slow}}^{\text{th}} \approx 0.78$.

C.5 Verdict

The 8×8 construction is the only physically valid spectral object for the continuous-time walk on the 4.8.8 graph. The 4-vertex construction was not diagonalising the identical adjacency matrix; it was diagonalising a chirally-broken, topologically aliased shadow of it in which the bipartite structure of the underlying graph was algebraically erased by sublattice aliasing on the main diagonal. The empirical OTOC centroid $(0.81, 0.60)$, the three-dip signature ($t_1 = 7$, $t_2 = 13$, $t_3 = 16$), and the $N = 3600$ bulk robustness are all measured directly from the bare adjacency matrix and remain unchanged across both constructions.

References

[1] X. Mi, P. Roushan, C. Quintana, S. Mandrà, et al., "Information scrambling in quantum circuits," *Science*, 374(6574):1479–1483, 2021.

[2] E. H. Lieb and D. W. Robinson, "The finite group velocity of quantum spin systems," *Communications in Mathematical Physics*, 28(3):251–257, 1972.

[3] K. Hashimoto, K. Murata, and R. Yoshii, "Out-of-time-order correlators in quantum mechanics," *Journal of High Energy Physics*, 2017(10):138, 2017.

[4] D. Aharonov, A. Ambainis, J. Kempe, and U. Vazirani, "Quantum walks on graphs," *Proceedings of the thirty-third annual ACM symposium on Theory of computing (STOC)*, 50–59, 2001.

[5] A. M. Childs, "Universal computation by quantum walk," *Physical Review Letters*, 102(18):180501, 2009.

[6] B. Grünbaum and G. C. Shephard, *Tilings and Patterns*. W.H. Freeman, 1987.

[7] S. Bravyi and A. Kitaev, "Universal quantum computation with ideal Clifford gates and noisy ancillas," *Physical Review A*, 71(2):022316, 2005.

@miscelliman2026code, author = Elliman, D., title = Code for "Lattice Birefringence on the 4.8.8 Walk Graph", year = 2026, url = https://github.com/dgedge/birefringence